Supplementary Information

P-O functional group anchoring Pt-Co electrocatalyst for high-durability PEMFCs

Sheng-Nan Hu [a], Wei-Cheng Xu [a], Na Tian [a,*], Su-Min Chen [a], Meng-Ying Li [b], Jun-Fei Shen [a], Jin-Xia Lin [a], Shuai-Long Guo [c], Xiao-Yang Huang [a,d], Zhi-You Zhou [a], Shi-Gang Sun [a,*]

[a] State Key Laboratory of Physical Chemistry of Solid Surfaces, Collaborative Innovation Center of Chemistry for Energy Materials, College of Chemistry and Chemical Engineering, Xiamen University, Xiamen 361005, China.

[b] Hubei Collaborative Innovation Center for Advanced Organic Chemical Materials & Key Laboratory for the Synthesis and Application of Organic Functional Molecules, Hubei University, Wuhan 430062, China.

[c] Singapore Centre for 3D Printing, School of Mechanical and Aerospace Engineering, Nanyang Technological University, 50 Nanyang Avenue, Singapore 639798, Singapore.

[d] Cardiff Catalysis Institute, School of Chemistry, Cardiff University, Main Building, Park Place, Cardiff, CF10 3AT, UK.

E-mail: tnsd@xmu.edu.cn; sgsun@xmu.edu.cn

Materials

All the chemical reagents were used as received from Sigma-Aldrich unless specified. These include platinum-(II) acetylacetonate ($Pt(acac)_2$, 97%), cobalt(II) acetylacetonate ($Co(acac)_2$, ⩾99.0%), phytic acid (PA, 70%), benzyl alcohol (BA, ⩾99.5%), N, N-dimethylformamide (DMF, ⩾99.9%), Pt/C (20 wt%, supported on Vulcan XC-72 black, Johnson Matthey) and Ketjen black carbon (KB, ECP-600JD, Japan LION). All the chemicals were used as received without further purification. The water (18.2 MΩ/cm) used in all experiments was prepared by passing through an ultra-pure purification system (Aqua Solutions).

Catalysts preparation

Synthesis of P_yO_x-KB supports

In a standard synthesis, phytic acid (PA) (5/10/20/50 μL) and KB (100 mg) were mixed in DMF (30 mL) and ultrasound for around 1h. The resulting homogeneous mixture was then put into a 50 mL Teflon-lined stainless steel autoclave and heated at 180 ℃ for 12 h, before it was cooled to room temperature. The resulting P_yO_x-KB products were collected by centrifugation and washed three times with an ethanol/acetone mixture.

To prepare the control sample of acid-treated KB (AT-KB), 1 g of KB was mixed with 100 mL 70% HNO_3 in a 250 mL round glass bottom flask. The suspension was immersed in a 70 °C preheated oil bath and continuously stirred under reflux for 5 h. After that, the AT-KB products were collected by centrifugation after washing with water until neutral.

Synthesis of PtCo/P_yO_x-KB catalysts

The PtCo/P_yO_x-KB catalysts were obtained by the further growth on the preformed P_yO_x-KB supports. In a typical preparation of PtCo/P_yO_x-KB catalysts, $Pt(acac)_2$ (2.0 mg), $Co(acac)_2$ (1.0 mg) and P_yO_x-KB (20 mg) prepared above were added in DMF (20 mL). The mixture was further added benzyl alcohol (1.0 mg) after magnetic stirring for around 30 minutes. After continued to be sonicated for around 2 h, the resulting mixture was put into a 50 mL Teflon-lined stainless steel autoclave and heated at 160 ℃ for 12 h before the mixture was naturally cooled to room temperature. The resulting PtCo/P_yO_x-KB catalysts were collected by centrifugation and washed three times with an ethanol/acetone mixture and annealed under Ar at 260 °C at a ramping rate of 10 °C min^{-1} for 1 h. PtCo/AT-KB was synthesized in the same as PtCo/P_yO_x-KB, except that P_yO_x-KB was replaced by AT-KB.

Characterization

Powder X-ray diffraction (XRD) patterns were collected on a Rigaku Ultima IV XRD with Cu-Kα radiation. X-ray photoelectron spectrum (XPS) was carried out on an Omicron SpheraII hemispherical electron energy analyzer with monochromatized Al Kα radiation (1486.6 eV). Themorphologies of the synthesized products were characterized through the scanning electron microscopy (SEM) collected by a Hitachi s-4800 instrument. The morphology and structure of the catalysts were characterized by transmission electron microscope (TEM) on JEM 1400, Tecnao F30, and condenser & aberration-corrected HAADF-STEM on JEM-ARM 300F at 200 kV. EELS mapping Gatan GIF Quantum 1077, 1.5 eV per channel on TEM FEI Talos F200X at 200 kV. In situ Raman spectra were obtained from an IDSPEC Confocal Raman Microscope with a 633 nm laser source. The Fourier transform infrared (FTIR) spectra were recorded by a Thermo Nicolet Nexus spectrometer. In situ FTIR spectroscopy experiments were

carried out on a Nicolet 8700 FTIR spectrometer (Thermo Scientific) equipped with a nitrogen cooled MCT-A defector using p-polarized light.

Electrochemical measurements

An open homemade electrochemical cell at 30 °C and a CHI 760E electrochemical workstation (Chenhua, Shanghai) with a RDE system (Pine Instruments) equipped with CHI-760E bipotentiostat was used for ORR electrolysis. The reference electrode was a saturated calomel electrode (SCE) and the counter electrode was a Pt foil. The working electrode was Pt/C or PtCo/P_yO_x-KB on glassy carbon rotating disk electrode (RDE, ϕ = 5 mm). To prepare the working electrode, 1 mg Pt/C or PtCo/P_yO_x-KB was dispersed in a mixture of water (0.45 mL), isopropanol (0.55 mL), and Nafion dispersion (5 wt%, 10 μL). The suspension was ultrasonicated for 2 h in an ice bath. To obtain a uniform thin catalyst film on the electrode, a 15 μL aliquot was dropped onto a glassy carbon rotating disk electrode (RDE, ϕ = 5 mm) and dried in the air, resulting in a Pt loading of 15.3 μg cm^{-2}. All of the measured potentials were converted to reversible hydrogen electrode (RHE) according to the Nernst equation ($E_{RHE} = E_{SCE} + 0.242 + 0.059$ pH). Before the ORR test, the electrode was electrochemically cleaned in N_2-saturated 0.1 M $HClO_4$ solution until a stable cyclic voltammogram was obtained. ORR was then tested by polarization curves between 0 and 1.1 V at 10 mV s^{-1} with a rotating rate of 1600 rpm in O_2-saturated 0.1 M $HClO_4$ solution. Accelerated durability tests (ADT) were performed at 30 °C by potential scanning between 0.6 and 1.0 V vs. RHE at a scan rate of 100 mV s^{-1} in O_2-saturated 0.1 M $HClO_4$. Up to 50,000 potential cycles were performed on the PtCo/$P_{2.73}O_x$-KB catalyst. Current densities were normalized by the geometric surface area and potentials were iR corrected.

The electrochemically active surface areas (ECSA) of catalysts were determined by calculating the charges associated with hydrogen underpotential deposition (H_{upd}) and then normalizing the results to the total mass of platinum loaded onto the catalyst.[1,2] The H_{upd} method measures the charge associated with the voltametric peaks for hydrogen adsorption, which is due to the attachment of one hydrogen atom on each metal atom on the surface.[3,4]

$$\text{ECSA} = \frac{Q_r}{C * m_{Pt}}$$

where m_{Pt} is the Pt mass loading, C is the charge of full monolayer coverage of H atoms onto clean polycrystalline Pt (210 μC cm^{-2}) and Q_r is the hydrogen adsorption charge in the negative-going scan during CV measurement.

According to the Koutechy–Levich equation, the kinectic current (J_k) could be obtained at 0.9V vs. RHE. The mass activity (MA) and specific activity (SA) were obtained by normalizing J_k at 0.9 V, regarding the loading of Pt and ECSA. The Koutecky-Levich equation was applied to derive J_k:

$$J_k = \frac{J * J_d}{J_d - J}$$

where J and J_d are the measured current and the diffusion limiting current, respectively.

XRD calculation method

The FWHM and crystallite sizes with the Gaussian fitting of the (111) diffraction peak were calculated using Debye–Scherrer and Bragg's Law expression shown in Eqs. 1 and 2:

$$d = \frac{k * \lambda}{W * cos\theta} \quad (1)$$

$$D_{(111)} = \frac{\lambda}{2 * sin\theta_{(111)}} \quad (2)$$

where d is the crystallite size (nm), $D_{(111)}$ is lattice spacing of (111) crystal faces, *k* is a constant (0.9 for spherical particles), λ is the wavelength of the X-ray radiation (CuKα = 0.1541 nm), *W* is the full width at half maximum (FWHM) of the intense and broad peaks, while θ is the diffraction angle (radian).

MEA preparation and fuel cell test

To prepare the MEA, 30 mg of Pt-based catalyst and 37.5 mg of 20 wt% Nafion solution were dispersed in a 10 mL mixture of isopropanol-water (4 : 1) using an ultrasonic process for 2 hours. The catalyst ink was then evenly coated on one side of a GORE-SELECT® membrane (12 μm) using ultrasonic spraying, with a cathode Pt loading of 0.10 mg_{Pt} cm^{-2}. The other side of the membrane was coated with a 20 wt% commercial Pt/C catalyst at a loading of 0.05 mg_{Pt} cm^{-2} as the anode. The electrode active area of MEA was 12.96 cm^2. Fuel cell data were collected using a Scribner 850e fuel cell test system under the following conditions: a cell temperature of 80 °C, a pressure of 50 KPa, and a gas flow of 2600 sccm and 600 sccm for air and H_2, respectively, at 100% relative humidity. Prior to conducting the polarization performance test, the MEA was activated using a constant-voltage step process. The fuel cell polarization test protocol involved multiple current steps, with each point being held for 2 min. For ADT in PEMFC, gas flow rates are 200 and 75 sccm for H_2 and N_2, respectively; potential steps are between 0.60 and 0.95 V with 3 s of holding time at each potential. After 30,000

cycles, the polarization curve of H_2-air PEMFC and mass activity of H_2-O_2 PEMFC were measured.

Density functional theory (DFT) calculations

First-principles calculations were carried out using density functional theory (DFT) with generalized gradient approximation (GGA) of Perdew-Burke-Ernzerhof (PBE) implemented in the Vienna Ab-Initio Simulation Package (VASP).[5,6] The valence electronic states were expanded on the basis of plane waves with the core-valence interaction represented using the projector augmented plane wave (PAW) approach and a cutoff of 520 eV.[7] A Γ-centered k-mesh of 2 × 2 × 1 was used for the surface calculations. Convergence is achieved when the forces acting on ions become smaller than 0.03 eV/Å. To calculate the formation energy (E_f), the following equation was used:

$$E_f = E_{PtCo/P_{2.73}O_x-KB} - E_{KB} - n_\alpha\mu_P - n_\beta\mu_O + (n_\alpha + n_\beta)\mu_C - n_\eta\mu_{Pt} - n_\theta\mu_{Co}$$

$$\mu_P = \frac{1}{n_P}E_P$$

$$\mu_O = \frac{1}{2}E_{O_2}$$

$$\mu_C = \frac{1}{n_C}E_C$$

where $E_{PtCo/P_{2.73}O_x-KB}$, E_C, E_P, and E_{O_2} are the total energy of PtCo/$P_{2.73}O_x$-KB, carbon support, bulk P, and gas-phase O_2, respectively. μ_P, μ_O, μ_C, μ_{Pt} and μ_{Co} are the related chemical potential of P, O, C, Pt (space group FM-3M), and Co (space group FM-3M), respectively. n_α, n_β, n_η, and n_θ are the number of P, O, Pt, and Co atoms in

PtCo/$P_{2.73}O_x$-KB, respectively. n_P is the number of P atoms in the most stable bulk structure of phosphorus. n_C is the number of C atoms in the carbon support.[8-10]

The adsorption sites for surface species have been pinpointed as the top Pt sites, given our model features PtCo (1:1) clusters with a Pt coating on the surface. We initially evaluated various high-symmetry sites by placing the cluster at an optimal distance from the surface. Subsequently optimizing it to its lowest energy configuration and the two configurations with similar energy are obtained.

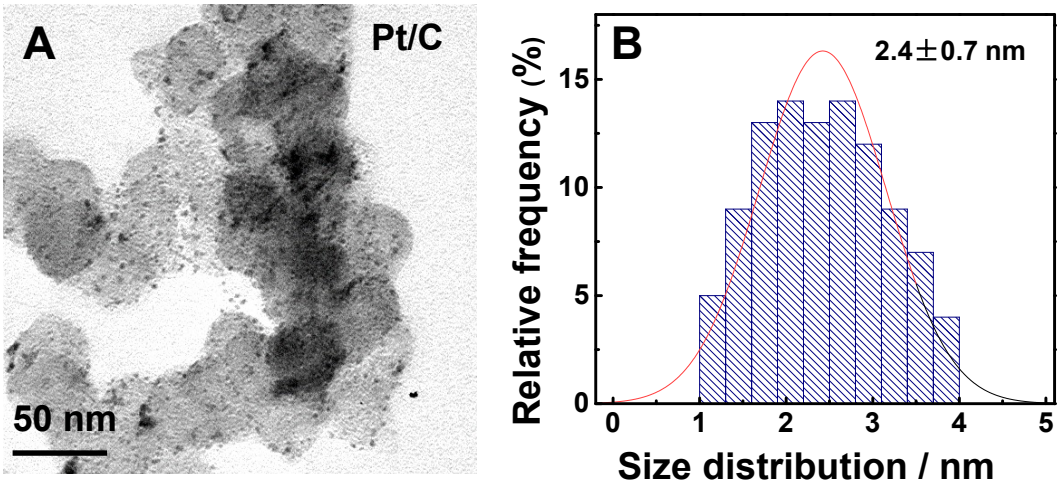

Fig. S1 (A) TEM images of commercial Pt/C and (B) the corresponding particle size histogram.

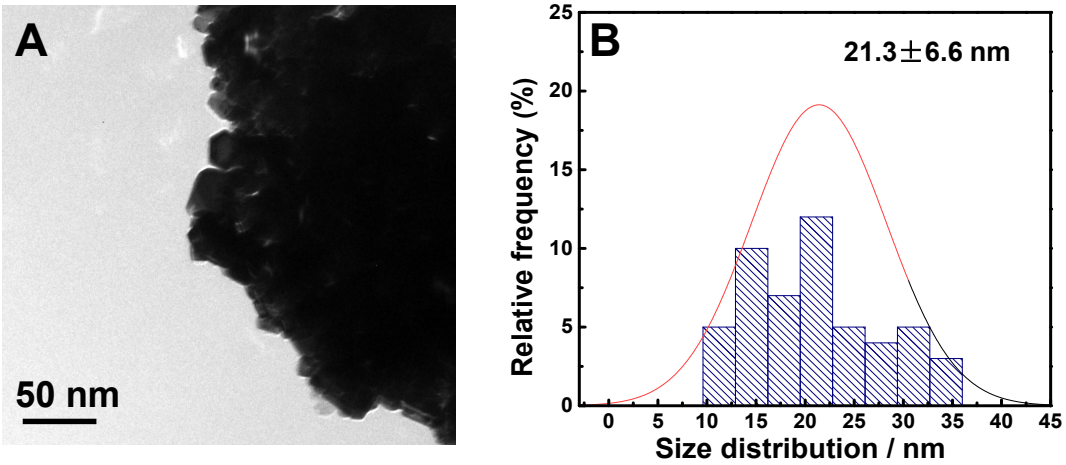

Fig. S2 (A) TEM images and (B) the corresponding particle size histogram of PtCo/PA synthesized with PA but without carbon support.

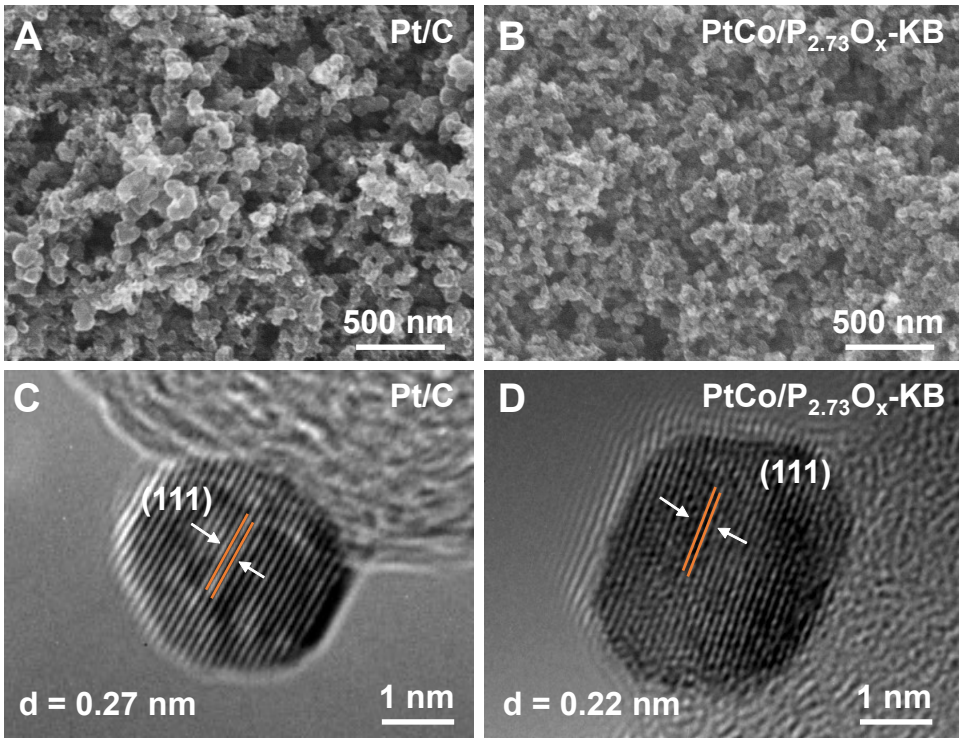

Fig. S3 SEM images of (A) commercial Pt/C and (B) PtCo/$P_{2.73}O_x$-KB. HRTEM images of (C) commercial Pt/C and (D) PtCo/$P_{2.73}O_x$-KB.

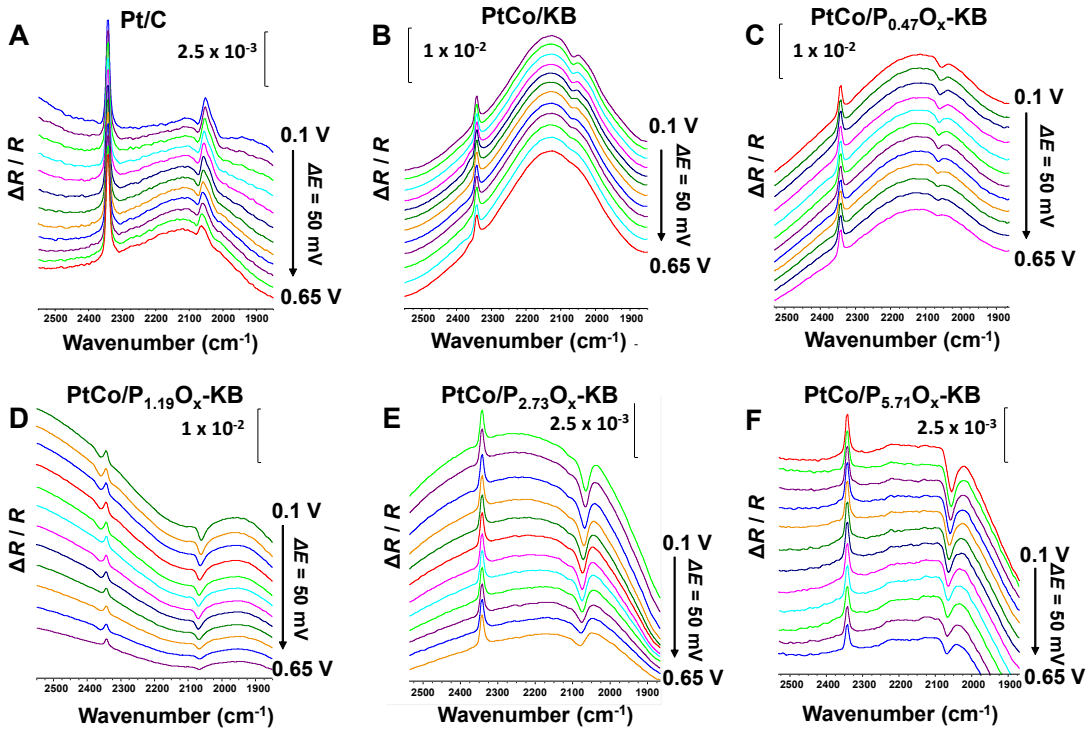

Fig. S4 In situ FTIR spectra of CO adsorbed on (A) Pt/C, (B) PtCo/KB, (C) PtCo/$P_{0.47}O_x$-KB, (D) PtCo/$P_{1.19}O_x$-KB, (E) PtCo/$P_{2.73}O_x$-KB, and (F) PtCo/$P_{5.71}O_x$-KB.

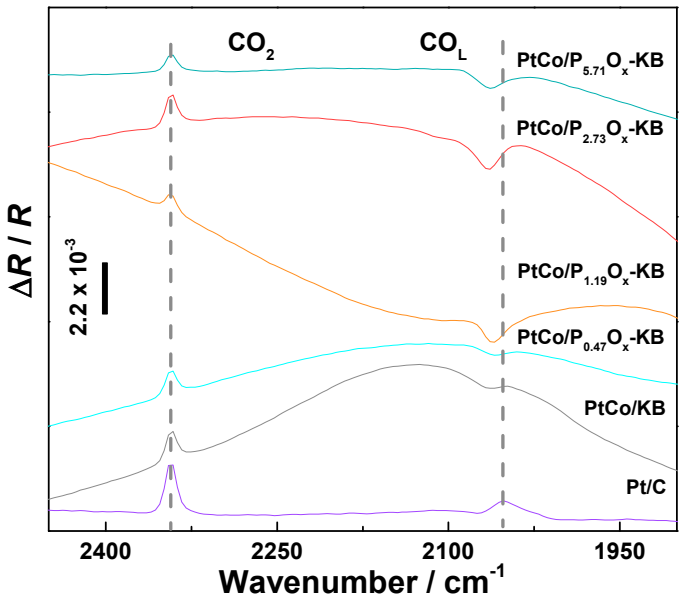

Fig. S5 Electrochemical in situ FTIR spectra of CO adsorbed on the as-prepared catalysts at 0.1 V.

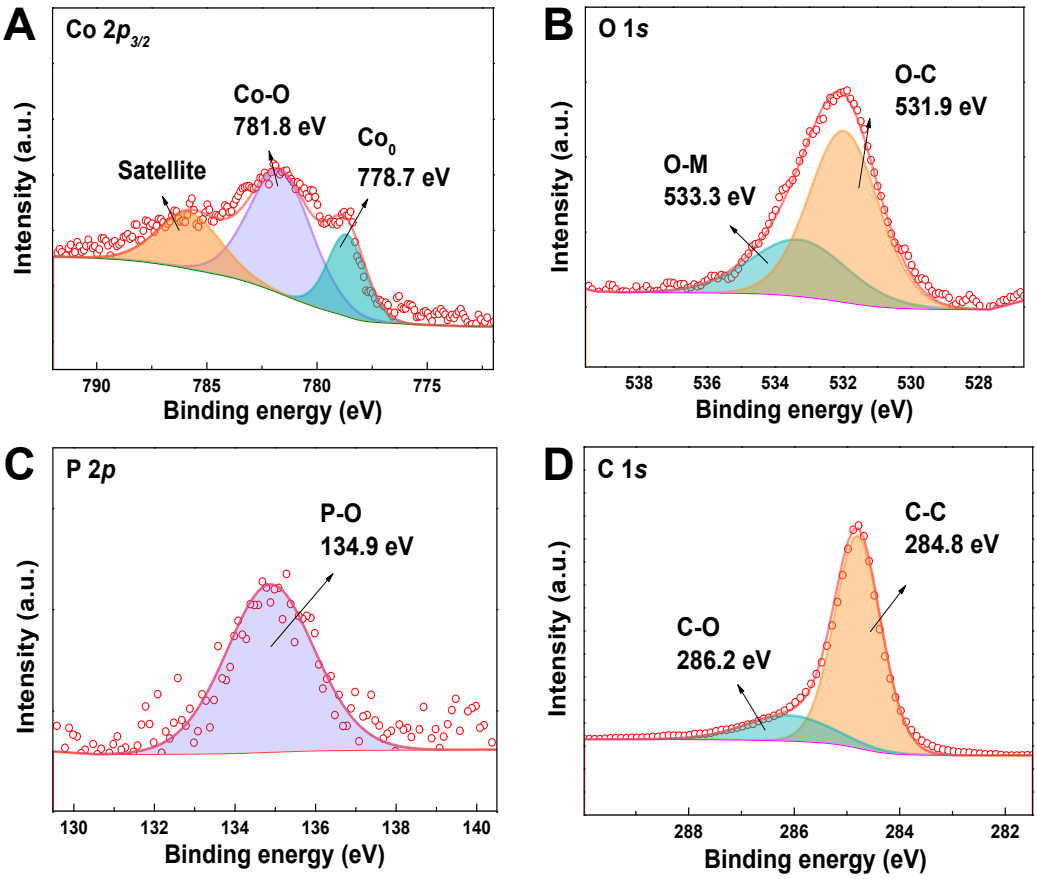

Fig. S6 XPS spectra of Co 2*p*, O 1*s*, P 2*p* and C 1*s* of PtCo/$P_{2.73}O_x$-KB.

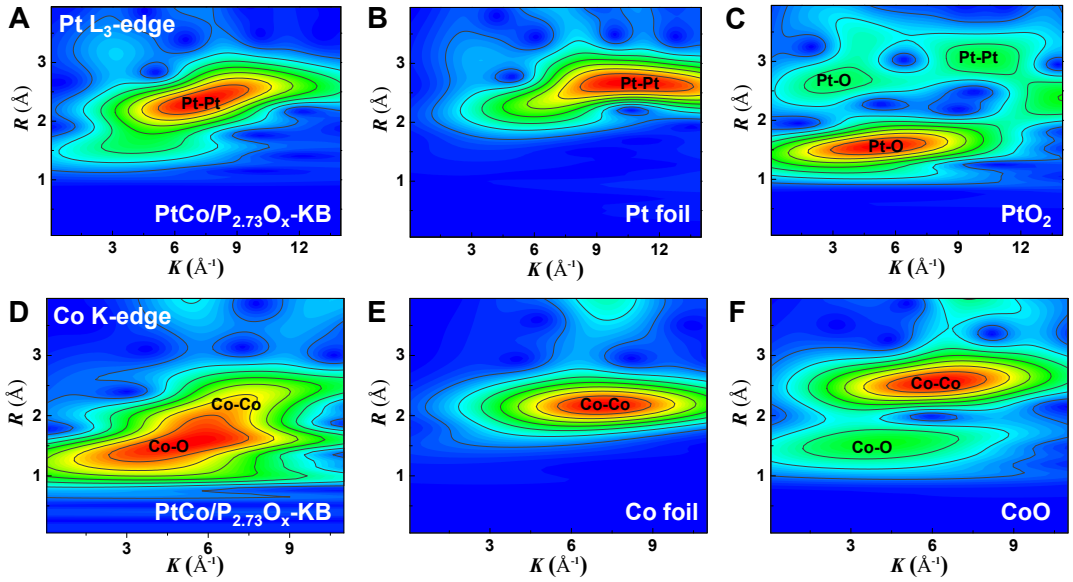

Fig. S7 Wavelet transform spectrum of Pt in (A) PtCo/$P_{2.73}O_x$-KB, (B) Pt foil and (C) PtO_2 as reference (FT range: 0.05-14 $Å^{-1}$); Wavelet transform spectra of Co in (D) PtCo/$P_{2.73}O_x$-KB, (E) Co foil and (F) CoO as reference (FT range: 0.05-11 $Å^{-1}$).

Table S1. EXAFS fitting parameters at the Pt L_3-edge for various samples (S_0^2=0.84).

	shell	CN	R(Å)	σ^2	ΔE_0	R factor
Pt foil	Pt-Pt	12	2.76±0.01	0.0047	7.4±0.3	0.0009
PtO_2	Pt-O	6.0±0.3	2.01±0.01	0.0028	13.0±0.7	0.0124
	Pt-Pt	7.6±0.7	3.11±0.01	0.0044		
	Pt-O	8.1±1.9	3.65±0.02	0.0040		
$PtCo/P_{2.73}O_x$-KB	Pt-O	0.2±0.1	1.96±0.01	0.0044	6.4±0.4	0.0015
	Pt-Co	2.1±0.1	2.66±0.01	0.0106		
	Pt-Pt	6.1±0.2	2.72±0.01	0.0071		

[a]*N*: coordination numbers; [b]*R*: bond distance; [c]σ^2: Debye-Waller factors; [d] ΔE_0: the inner potential correction. *R* factor: goodness of fit.

Table S2 EXAFS fitting parameters at the Co K-edge for various samples (S_0^2=0.76).

	shell	CN	R(Å)	σ^2	ΔE_0	R factor
Co foil	Co-Co	12	2.49±0.01	0.0065	7.4±0.3	0.0009
CoO	Co-O	6.3±0.8	2.10±0.01	0.0096	13.0±0.7	0.0124
	Co-Co	12.4±0.7	3.01±0.01	0.0079		
	Co-O	4.3±0.3	2.09±0.02	0.0103		
PtCo/$P_{2.73}O_x$-KB	Co-O	4.3±0.3	2.09±0.02	0.0103	2.6±2.8	0.0071
	Co-Pt	1.0±0.3	2.72±0.02	0.0041		
	Co-Co	2.4±0.4	2.65±0.03	0.0119		

[a]*N*: coordination numbers; [b]*R*: bond distance; [c]σ^2: Debye-Waller factors; [d] ΔE_0: the inner potential correction. *R* factor: goodness of fit.

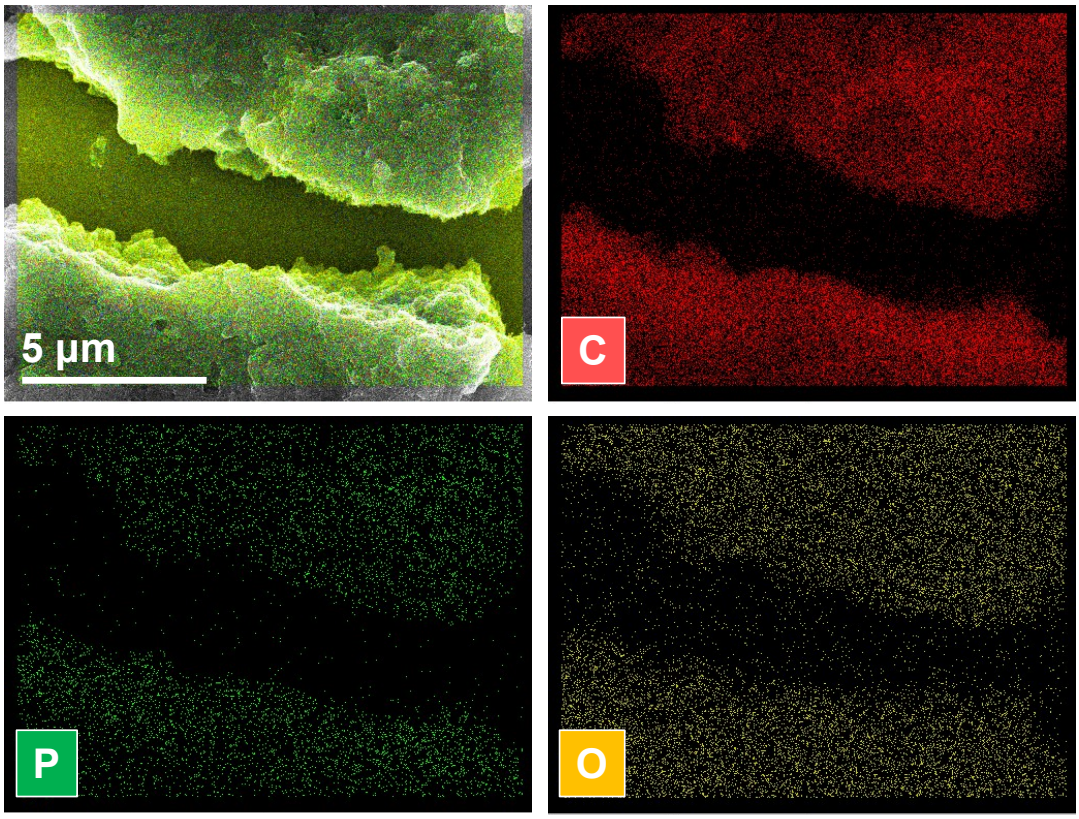

Fig. S8 SEM-EDS mapping of the $P_{2.73}O_x$-KB.

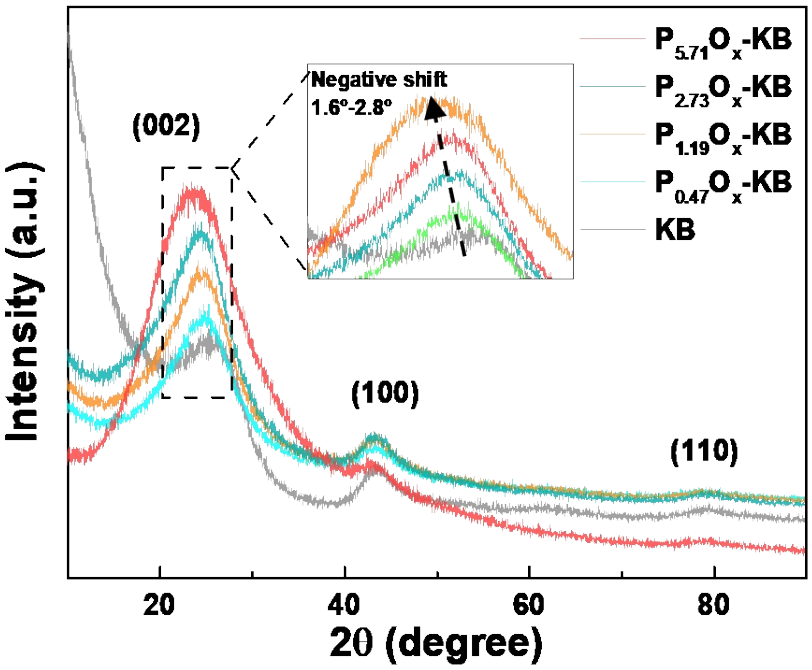

Fig. S9 XRD pattern of P_yO_x-KB.

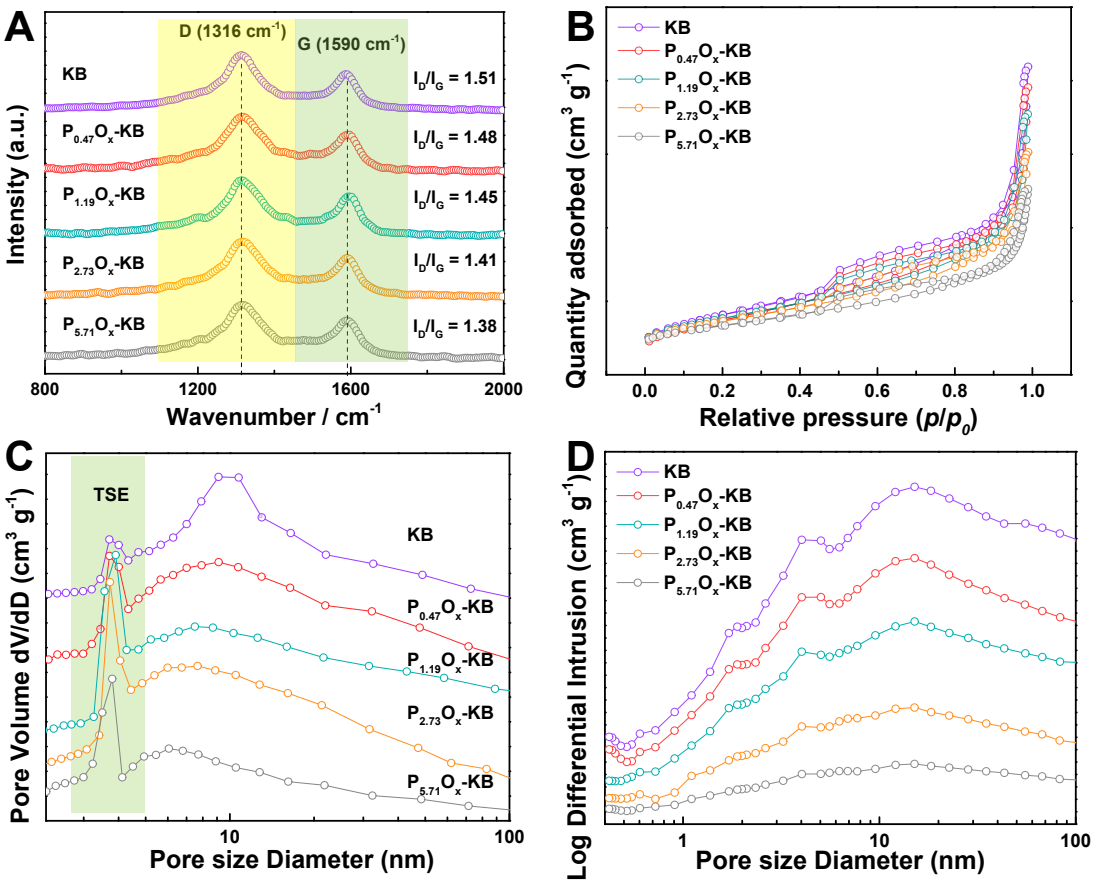

Fig. S10 (A) Raman spectra, (B) N_2 adsorption-desorption isotherms, (C) Barret-Joyner-Halenda (BJH) and (D) Mercury-Intrusion-Porosimetry (MIP) pore size distribution of KB and P_yO_x-KB.

Table S3. I_D/I_G from Raman spectra, BET surface area, BJH and MIP average pore size distribution of KB and P_yO_x-KB.

	I_D/I_G	BET surface area (cm^2 g^{-1})	BJH average pore size (nm)	MIP average pore size (nm)
KB	1.51	1593	11.6	13.2
$P_{0.47}O_x$-KB	1.48	1529	10.3	12.2
$P_{1.19}O_x$-KB	1.45	1463	9.8	11.6
$P_{2.73}O_x$-KB	1.41	1292	8.9	9.8
$P_{5.71}O_x$-KB	1.38	1034	8.3	9.2

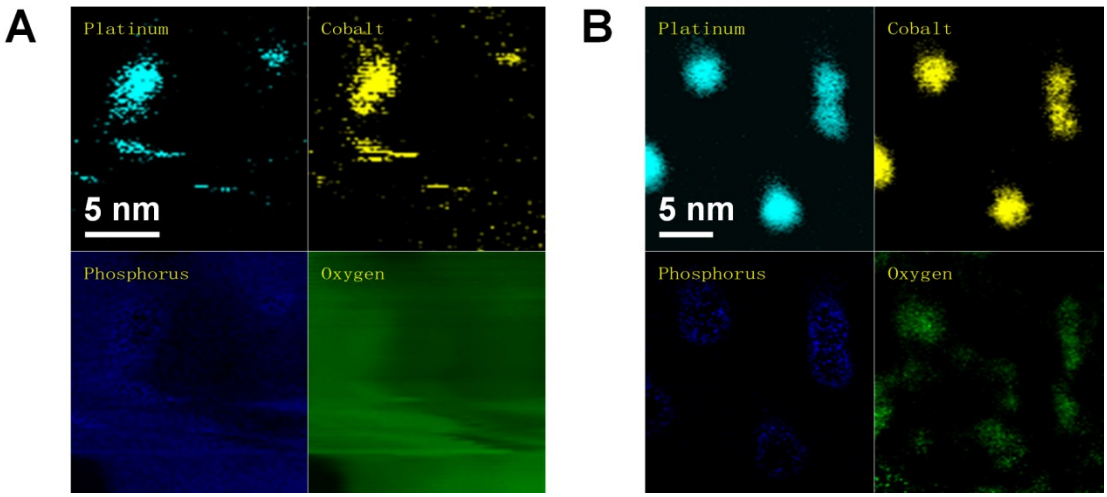

Fig. S11 EELS mapping images of the PtCo/$P_{2.73}O_x$-KB (A) before and (B) after annealing at 1000 °C for 1 hour.

Table S4 Element content of the as-prepared catalysts measured by ICP-MS.

	Pt (wt%)	**Co (wt%)**	**P (wt%)**	**Atomic ratio of Pt/Co**
Pt/C	19.82	/	/	/
PtCo/KB	16.71	5.05	/	0.98
PtCo/$P_{0.47}O_x$-KB	17.24	4.61	0.34	1.13
PtCo/$P_{1.19}O_x$-KB	18.85	5.56	0.71	1.02
PtCo/$P_{2.73}O_x$-KB	18.21	5.66	1.77	0.96
PtCo/$P_{5.71}O_x$-KB	19.13	5.83	3.36	0.99

Table S5 Element content of the as-prepared catalysts measured by XPS.

	Pt (at%)	**Co (at%)**	**P (at%)**	**Pt/Co**
Pt/C	2.36	/	/	/
PtCo/KB	0.68	0.33	/	2.06
PtCo/$P_{0.47}O_x$-KB	0.91	0.35	0.41	2.58
PtCo/$P_{1.19}O_x$-KB	1.14	0.42	0.46	2.73
PtCo/$P_{2.73}O_x$-KB	1.5	0.56	0.53	2.68
PtCo/$P_{5.71}O_x$-KB	2.03	0.85	0.78	2.39

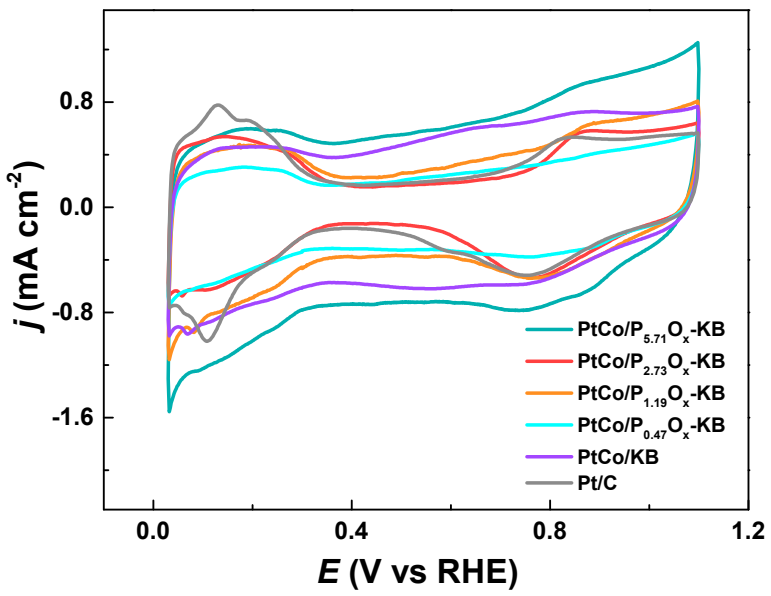

Fig. S12 CV curves of Pt/C, PtCo/KB, PtCo/$P_{0.47}O_x$-KB, PtCo/$P_{1.19}O_x$-KB, PtCo/$P_{2.73}O_x$-KB, and PtCo/$P_{5.71}O_x$-KB.

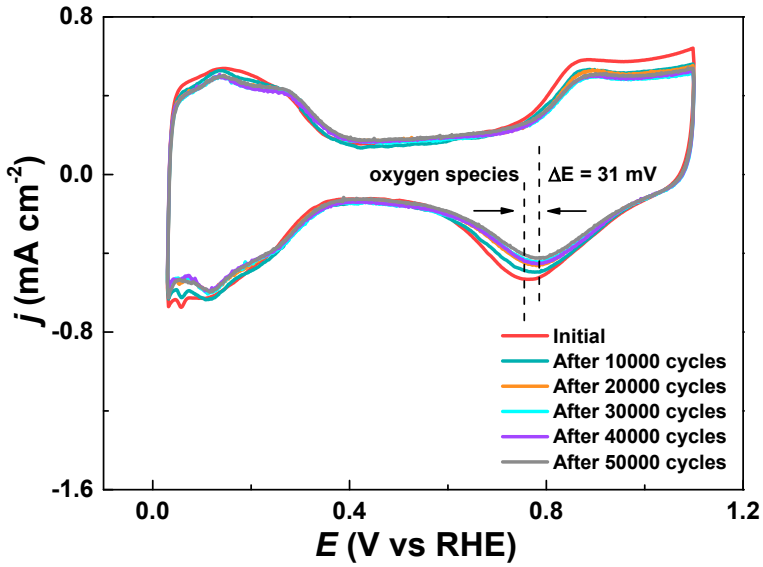

Fig. S13 CV curves of PtCo/$P_{2.73}O_x$-KB before and after ADT.

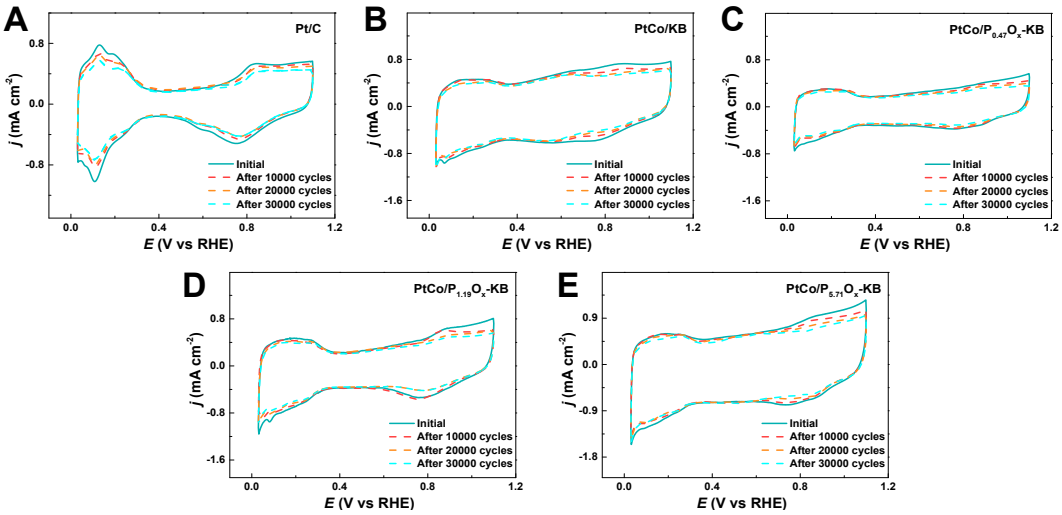

Fig. S14 CV curves of (A) Pt/C, (B) PtCo/KB, (C) PtCo/$P_{0.47}O_x$-KB, (D) PtCo/$P_{1.19}O_x$-KB, and (E) PtCo/$P_{5.71}O_x$-KB before and after ADT.

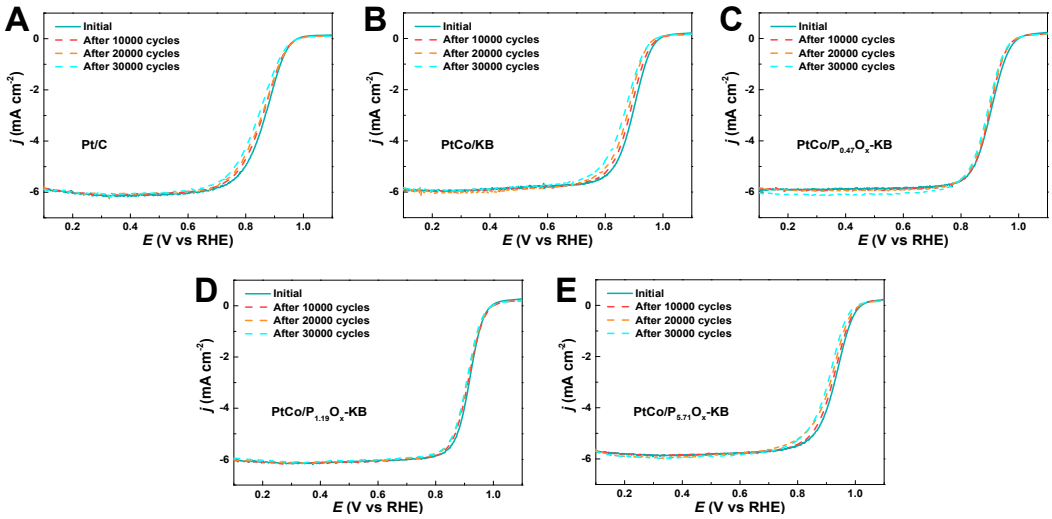

Fig. S15 Polarization curves of (A) Pt/C, (B) PtCo/KB, (C) PtCo/$P_{0.47}O_x$-KB, (D) PtCo/$P_{1.19}O_x$-KB, and (E) PtCo/$P_{5.71}O_x$-KB before and after ADT.

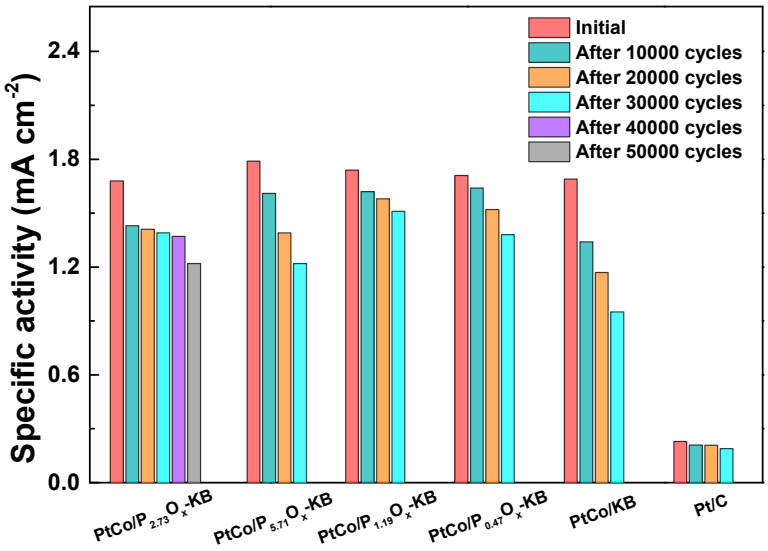

Fig. S16 Specific activity of Pt/C, PtCo/KB, PtCo/$P_{0.47}O_x$-KB, PtCo/$P_{1.19}O_x$-KB, PtCo/$P_{2.73}O_x$-KB and PtCo/$P_{5.71}O_x$-KB before and after ADT.

Table S6 Comparison of the ORR performance at 0.9 V in 0.1 M $HClO_4$ on recent reported PtCo-based catalysts.

Catalysts	Pt loading (μg_{Pt} cm^{-2})	SA (mA cm^{-2})	MA (A mg_{Pt}^{-1})	MA loss after 30k ADT (%)	Refs.
PtCo/$P_{2.73}O_x$-KB	13.93	1.68	1.11	24.3	This work
$L1_0$-PtCo/NC	17.6	1.11	1.27	37	11
A1- PtCo/NC	15.4	1.07	1.42	62.7	
PtCoNMC	18.75	0.84	0.956	19	12
PtCo/Co-N-C	12.14	--	0.7	44.43	13
Pt-Co ND-NF	23	2.624	0.939	44.8	14
Pt-Co-Mo-I	5.44	--	0.71	32	15
PtCo/CNT	16	--	0.469	29.18	16
Pt-rich PtCo NFs	35.71	11.23	2.63	55.89	17
PtCo NFs	35.71	1.16	0.59	66.1	
STG-assisted PtCo	11-13	--	1.08	25	18
Umic-30 wt% PtCo	11-13	--	0.86	33	

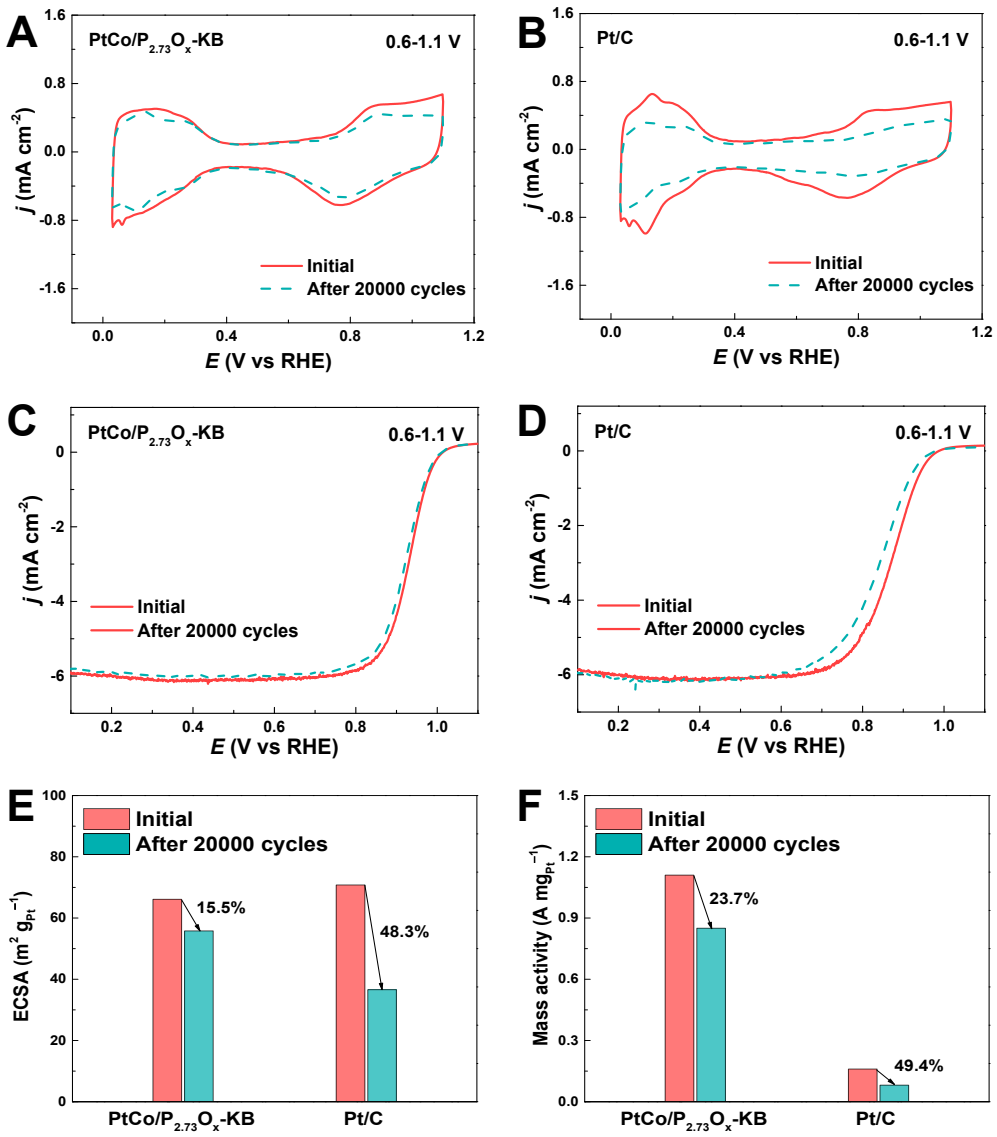

Fig. S17 CV curves of (A) PtCo/$P_{2.73}O_x$-KB and (B) Pt/C. ORR polarization curves of (C) PtCo/$P_{2.73}O_x$-KB and (D) Pt/C; (E) ECSA and (F) Mass activity of PtCo/$P_{2.73}O_x$-KB and Pt/C before and after 20,000 potential cycles between 0.6 and 1.1 V at 100 mV s^{-1}.

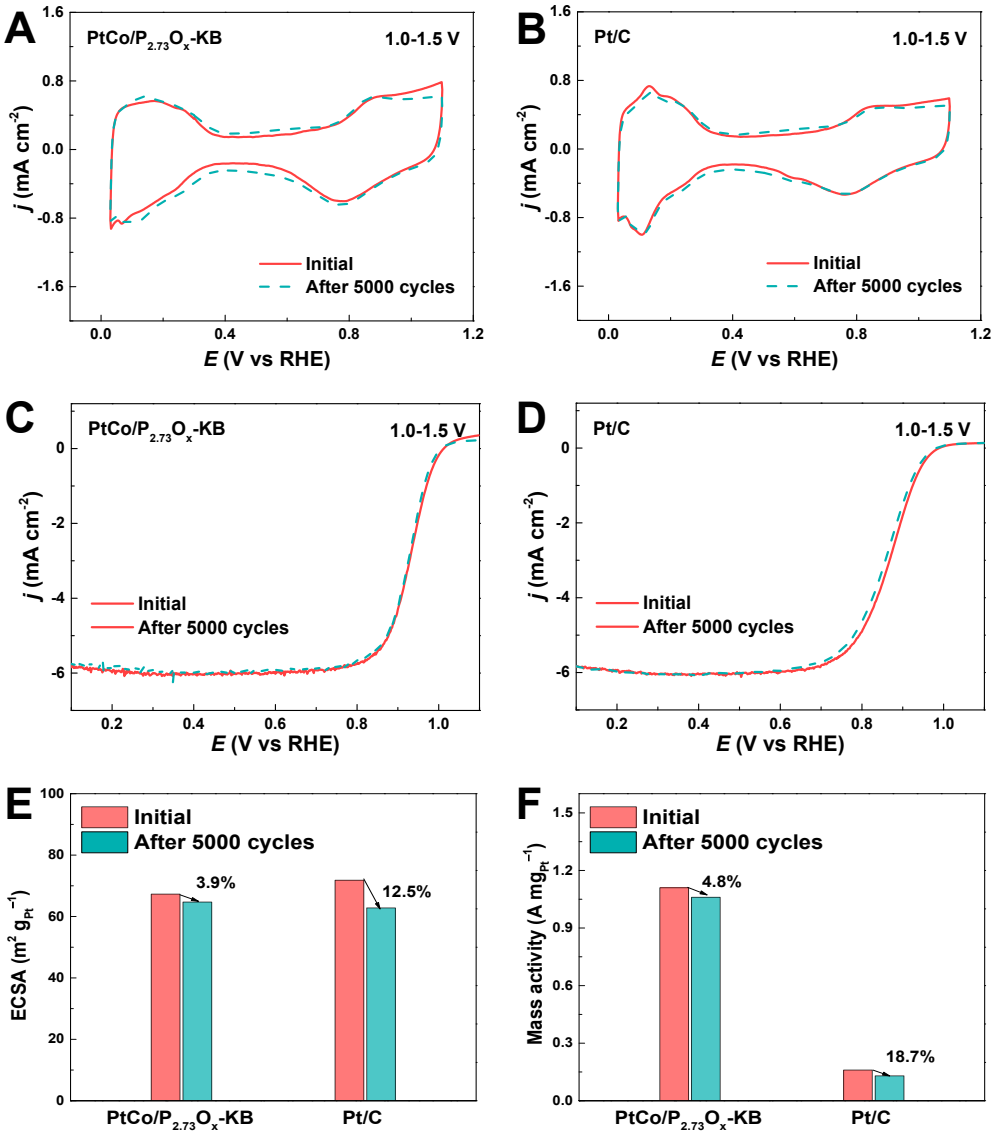

Fig. S18 CV curves of (A) PtCo/$P_{2.73}O_x$-KB and (B) Pt/C in 0.1 M $HClO_4$. ORR polarization curves of (C) PtCo/$P_{2.73}O_x$-KB and (D) Pt/C; (E) ECSA and (F) Mass activity of PtCo/$P_{2.73}O_x$-KB and Pt/C before and after 5,000 potential cycles between 1.0 and 1.5 V at 500 mV s^{-1}.

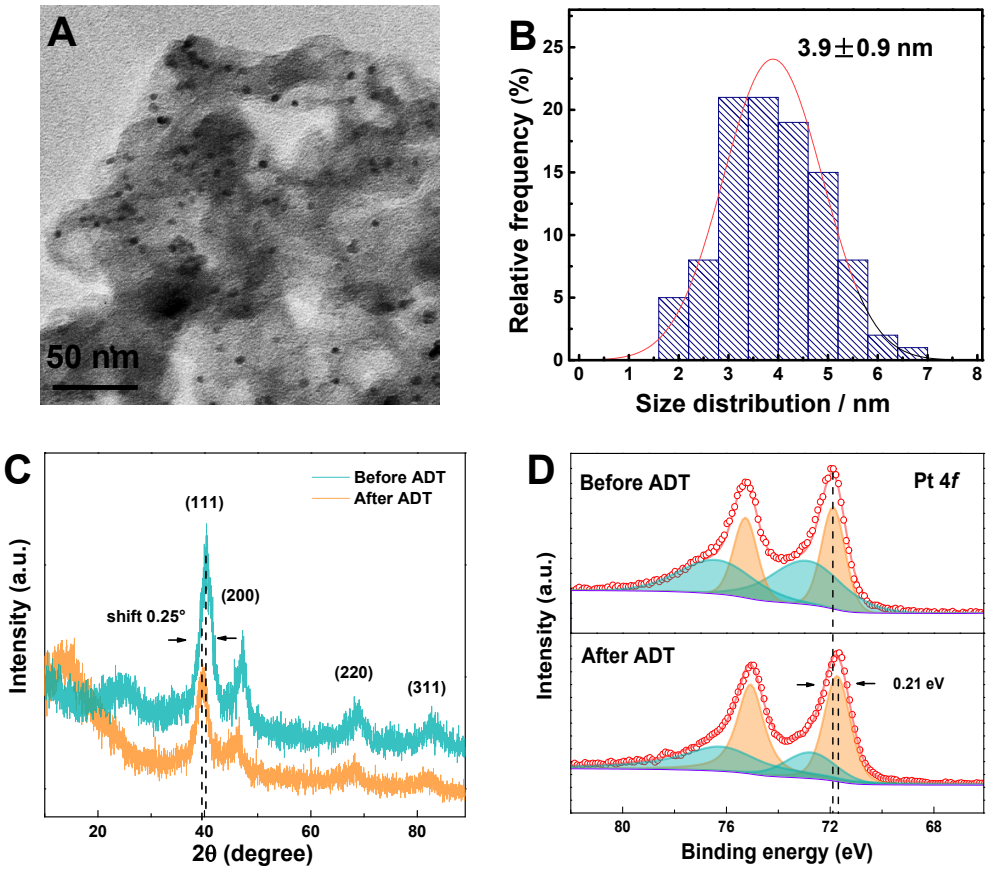

Fig. S19 (A) TEM images, (B) the corresponding particle size histogram, (C) XRD pattern and (D) XPS spectra of PtCo/$P_{2.73}O_x$-KB before and after 50000 cycles.

Table S7 Element content of PtCo/$P_{2.73}O_x$-KB after 50000 cycles measured by ICP-MS.

	ICP-MS
Pt	8.79 wt%
Co	0.96 wt%
P	1.09 wt%
Atomic ratio of Pt/Co	2.77

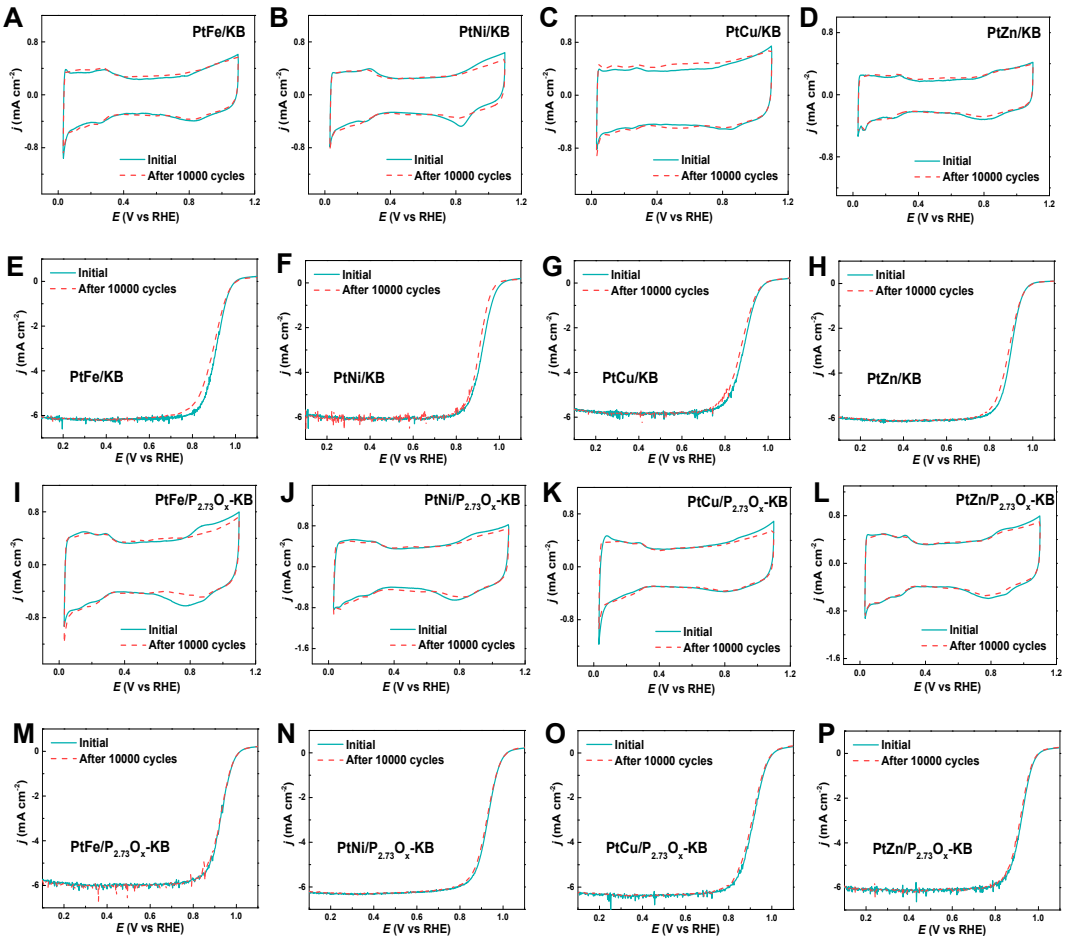

Fig. S20 CV curves of (A) PtFe/KB, (B) PtNi/KB, (C) PtCu/KB, (D) PtZn/KB, (I) PtFe/$P_{2.73}O_x$-KB, (J) PtNi/$P_{2.73}O_x$-KB, (K) PtCu/$P_{2.73}O_x$-KB, and (L) PtZn/$P_{2.73}O_x$-KB after 10000 potential cycles. Polarization curves of (E) PtFe/KB, (F) PtNi/KB, (G) PtCu/KB, (H) PtZn/KB, (M) PtFe/$P_{2.73}O_x$-KB, (N) PtNi/$P_{2.73}O_x$-KB, (O) PtCu/$P_{2.73}O_x$-KB, and (P) PtZn/$P_{2.73}O_x$-KB after 10000 potential cycles.

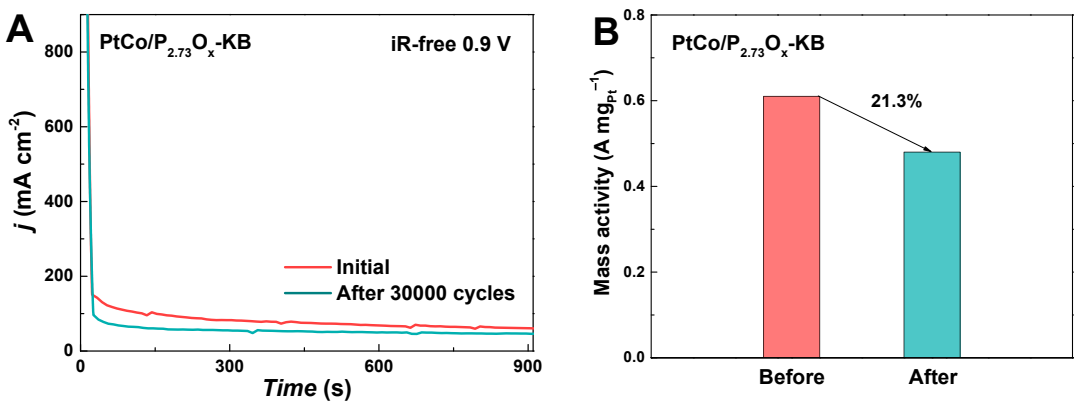

Fig. S21 (A) Current-time curve of H_2-O_2 PEMFC with PtCo/$P_{2.73}O_x$-KB as the cathode at 0.9 V. (B) iR-free mass activity of PtCo/$P_{2.73}O_x$-KB at 0.9 V before and after the ADT of 30,000 square-wave potential cycles between 0.60 and 0.95 V. The holding time at each potential was 3.0 s..

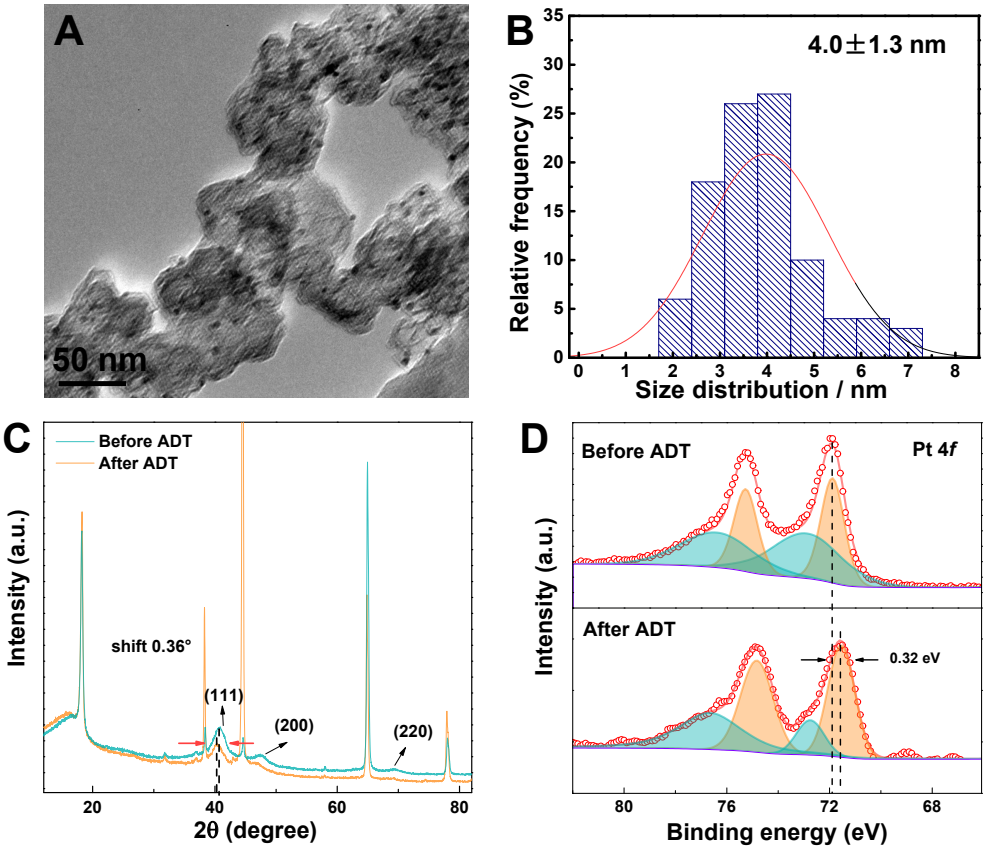

Fig. S22 (A) TEM images and (B) the corresponding particle size histogram of PtCo/$P_{2.73}O_x$-KB after 30,000 cycles of ADT in PEMFC. (C) XRD pattern and (D) XPS spectra of PtCo/$P_{2.73}O_x$-KB before and after 30,000 cycles of ADT in PEMFC. Sharp diffraction peaks in (C) come from GORE-SELECT PEM membrane and Nafion ionomer.

Table S8 Element content of PtCo/$P_{2.73}O_x$-KB after 30,000 cycles of ADT in PEMFC measured by ICP-MS.

	ICP-MS
Pt	7.12 wt%
Co	0.71 wt%
P	1.12 wt%
Atomic ratio of Pt/Co	3.03

Table S9 Element content of the as-prepared catalysts measured by ICP-MS.

	Pt (wt%)	**M (wt%)**
PtFe/KB	18.11	Fe (4.93)
PtNi/KB	17.74	Ni (5.62)
PtCu/KB	15.88	Cu (4.02)
PtZn/KB	17.95	Zn (5.28)
PtFe/$P_{2.73}O_x$-KB	16.87	Fe (4.72)
PtNi/$P_{2.73}O_x$-KB	19.59	Ni (6.04)
PtCu/$P_{2.73}O_x$-KB	15.56	Cu (4.16)
PtZn/$P_{2.73}O_x$-KB	18.33	Zn (5.94)

Table S10 Comparison of the H_2-air PEMFC performance on recent reported PtCo-based catalysts.

Catalysts	Pt loading (mg_{Pt} cm^{-2})	Outlet pressure (kPa)	Active area (cm^2)	Peak power density (W cm^{-2})	Cell voltage loss after 30k ADT (mV)	Refs.
PtCo/$P_{2.73}O_x$-KB	0.05/0.1	50	12.96	1.21	0	This work
$Ga_{0.1}$-PtCo	0.025/0.075	50	5	1.2	27	19
PtCo@Gnp	0.01/0.09	50	5	1.01	23.5	20
$L1_0$-W-PtCo/C	--	50	--	--	30	21
PtCoNWs	0.025/0.05	50	5	1.016	59	22
Sub-Pt_3Co-MC	0.2/0.2	150	1.44	0.8	45	23
PtCo/C3	0.05/0.1	50	--	1.16	16.9	24
i-CoPt@Pt/KB	0.1/0.1	50	5.06	1.18	29	25
Pt−Co/C(com)	--	150	5	1.818	35	26

Table S11 The 2 theta and full width at half maximum (FWHM) of in-situ XRD on Pt/C, PtCo/KB and PtCo/$P_{2.73}O_x$-KB.

	Pt/C	**PtCo/KB**	**PtCo/$P_{2.73}O_x$-KB**
Initial (2 theta)	39.660°	40.421°	40.427°
Initial (FWHM)	3.120	1.981°	2.097°
After 1,000 cycles (2 theta)	39.660°	40.334°	40.365°
After 1,000 cycles (FWHM)	2.238°	1.786°	2.073°
After 2,000 cycles (2 theta)	39.660°	40.202°	40.211°
After 2,000 cycles (FWHM)	2.038°	1.716°	2.057°
After 3,000 cycles (2 theta)	39.660°	40.161°	40.167°
After 3,000 cycles (FWHM)	1.961°	1.705°	2.021°
After 4,000 cycles (2 theta)	39.660°	40.073°	40.132°
After 4,000 cycles (FWHM)	1.933°	1.691°	1.997°
After 5,000 cycles (2 theta)	39.660°	40.035°	40.040°
After 5,000 cycles (FWHM)	1.848°	1.669°	1.972°

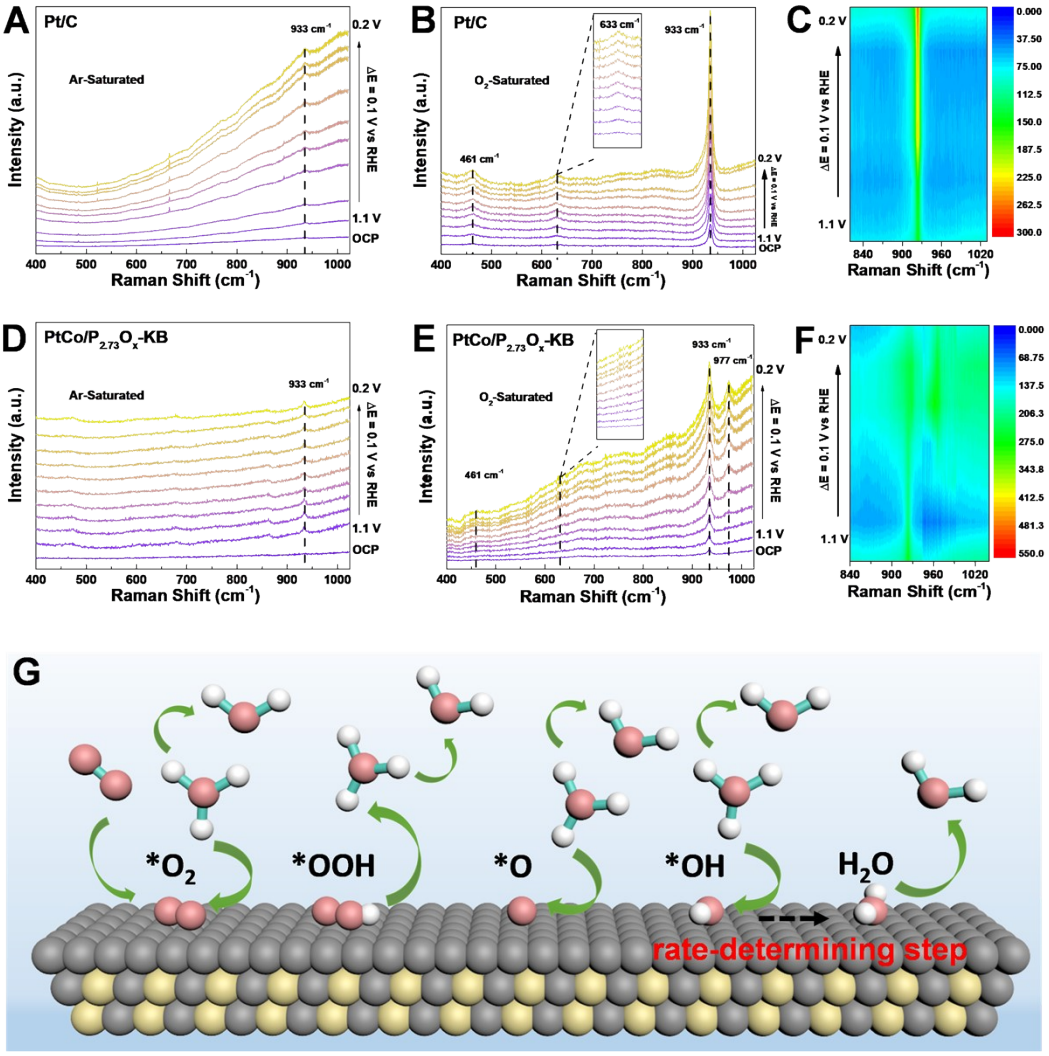

Fig. S23 In-situ Raman spectroscopy of Pt/C (A) saturated with Ar, (B) saturated with O_2 and (C) the corresponding 2D spectra. In-situ Raman spectroscopy of PtCo/$P_{2.73}O_x$-KB (D) saturated with Ar, (E) saturated with O_2 and (F) the corresponding 2D spectra in 0.1 M $HClO_4$ solution. (G) Schematic diagram of the ORR reaction pathway of PtCo/$P_{2.73}O_x$-KB; the gray, yellow, red, and white balls represent Pt, Co, O, and H atoms, respectively.

References

1. M. Li, Z. Zhao, T. Cheng, A. Fortunelli, C. Y. Chen, R. Yu, Q. Zhang, L. Gu, B. Merinov, Z. Lin, E. Zhu, T. Yu, Q. Jia, J. Guo, L. Zhang, W. A. Goddard, Y. Huang and X. Duan, Ultrafine jagged platinum nanowires enable ultrahigh mass activity for the oxygen reduction reaction, *Science,* 2016, **354**, 1414.
2. Z. Yang, H. Yang, L. Shang and T. Zhang, Ordered PtFeIr intermetallic nanowires prepared through a silica-protection strategy for the oxygen reduction reaction, *Angew. Chem. Int. Ed.,* 2022, **61**, e202113278.
3. S. Zhao, H. Yu, R. Maric, N. Danilovic, C. B. Capuano, K. E. Ayers and W. E. Mustain, Calculating the electrochemically active surface area of iridium oxide in operating proton exchange membrane electrolyzers, *J. Electrochem. Soc.,* 2015*,* **162**, F1292.
4. S. B. Brummer, J. I. Ford and M. J. Turner, The adsorption and oxidation of hydrocarbons on noble metal, *J. Phys. Chem. C.,* 1965, **69**, 3424.
5. K. Furthmuller, Efficient iterative schemes for ab initio total-energy calculations using a plane-wave basis set, *Phys. rev. B,* 1996*,* **54**, 11169.
6. J. P. Perdew, K. Burke and M. Ernzerhof, Generalized gradient approximation made simple, *Phys. Rev. Lett.,* 1998*,* **77**, 3865.
7. P. E. Bloch, Projector augmented-wave method, *Physical review. B, Condensed matter.,* 1994, **50**, 17953.
8. D. Galyamin, J. Torrero and I. Rodríguez, Active and durable R_2MnRuO_7 pyrochlores with low Ru content for acidic oxygen evolution, *Nat Commun.*, 2023, **14**, 2010.
9. A. Li, S. Kong, C. Guo, H. Ooka and K. Adachi, Enhancing the stability of cobalt spinel oxide towards sustainable oxygen evolution in acid, *Nat Catal.*, 2022, **5**, 109.

10. W. Zhu, X. Song, F. Liao, H. Huang, Q. Shao and K. Feng, Stable and oxidative charged Ru enhance the acidic oxygen evolution reaction activity in two-dimensional ruthenium-iridium oxide, *Nat Commun.*, 2023, **14**, 5365.
11. M. J. Wang, M. Wang, L. Guo, Y. Li, S. G. Chen and Z. D. Wei, Coating layer-free synthesis of sub-4 nm ordered intermetallic $L1_0$-PtCo catalyst for the oxygen reduction reaction, *Int. J. Hydrogen Energy,* 2022, **47**, 27116.
12. Z. Y. Chen, C. Hao, B. W. Yan, Q. Y. Chen, H. Y. Feng, X. Q. Mao, J. M. Cen, Z. Q. Tian, P. Tsiakaras and P. K. Shen, ZIF-$Mg(OH)_2$ dual template assisted self-confinement of small PtCo NPs as promising oxygen reduction reaction in PEM fuel cell, *Adv. Energy Mater.,* 2022, **12**, 2201600.
13. P. Guo, Y. F. Xia, B. Liu, M. Ma, L. X. Shen, Y. K. Dai, Z. Y. Zhang, Z. G. Zhao, Y. L. Zhang, L. Zhao and Z. B. Wang, Low-loading sub-3 nm PtCo nanoparticles supported on Co-N-C with dual effect for oxygen reduction reaction in proton exchange membrane fuel cells, *ACS Appl. Mater. Interfaces,* 2022, **14**, 53819.
14. X. X. Zhu, L. Huang, M. Wei, P. Tsiakaras and P. K. Shen. Highly stable Pt-Co nanodendrite in nanoframe with Pt skin structured catalyst for oxygen reduction electrocatalysis, *Appl. Catal. B-Environ.,* 2021, **281**, 119460.
15. L. C. Lin, C. H. Kuo, Y. H. Hsu, L. C. Hsu, H. Y. Chen, J. L. Chen and Y. T. Pan, High-performance intermetallic PtCo oxygen reduction catalyst promoted by molybdenum, *Appl. Catal. B-Environ.,* 2022, **317**, 121767.
16. F. Cao, H. Y. Zhang, X. Duan, X. K. Li, R. Ding, K. Hua, Z. Y. Rui and Y. K. Wu, Coating porous TiO_2 films on carbon nanotubes to enhance the durability of ultrafine PtCo/CNT nanocatalysts for the oxygen reduction reaction, *ACS Appl. Mater. Interfaces,* 2022, **14**, 51975.

17. M. Wei, L. Huang, L. B. Li, F. Ai, J. Z. Su and J. Wang, Coordinatively unsaturated PtCo flowers assembled with ultrathin nanosheets for enhanced oxygen reduction, *ACS Catal,.* 2022, **12**, 6478.

18. T. W. Song, C. Xu, Z. T. Sheng, H. K. Yan, L. Tong, J. Liu, W. J. Zeng, L. J. Zuo, P. Yin, M. Zuo, S. Q. Chu, P. Chen and H. W. Liang, Small molecule-assisted synthesis of carbon supported platinum intermetallic fuel cell catalysts, *Nat. Commun.,* 2022*,* **13**, 6521.

19. R. Y. Shao, X. C. Xu, Z. H. Zhou, W. J. Zeng, T. W. Song, P. Yin, A. Li, C. S. Ma, L. Tong, Y. Kong, H. W. Liang, Promoting ordering degree of intermetallic fuel cell catalysts by low-melting-point metal doping, Nat. Commun., **2023***, 14*, 5896.

20. Z. P. Zhao, Z. Y. Liu, A. Zhang, X. X. Yan, W. Xue, B. Peng, H. L. L. Xin, X. Q. Pan, X. F. Duan and Y. Huang, Graphene-nanopocket-encaged PtCo nanocatalysts for highly durable fuel cell operation under demanding ultralow-Pt-loading conditions, *Nat. Nanotechnol.,* 2022, **17**, 968.

21. J. S. Liang, N. Li, Z. L. Zhao, L. Ma, X. M. Wang, S. Z. Li, X. Liu, T. Y. Wang, Y. P. Du, G. Lu, J. T. Han, Y. H. Huang, D. Su and Q. Li, Tungsten-doped $L1_0$-PtCo ultrasmall nanoparticles as a high-performance fuel cell cathode, *Angew. Chem. Int. Ed.,* 2019, **131**, 15617.

22. J. Huang, B. S. Peng, T. Stracensky, Z. Y. Liu, A. Zhang, M. J. Xu, Y. Liu, Z. P. Zhao, X. F. Duan, Q. Y. Jia and Y. Huang, 1D PtCo nanowires as catalysts for PEMFCs with low Pt loading, *Sci. China Mater.,* 2022, **65**, 704.

23. H. Cheng, R. J. Gui, H. Yu, C. Wang, S. Liu, H. F. Liu, T. P. Zhou, N. Zhang, X. S. Zheng, W. S. Chu, Y. Lin, H. A. Wu, C. Z. Wu and Y. Xie, Subsize Pt-based

intermetallic compound enables long-term cyclic mass activity for fuel-cell oxygen reduction, *PNAS,* 2021, **118**, e2104026118.

24. Z. P. Zhao, M. D. Hossain, C. C. Xu, Z. J. Lu, Y. S. Liu, S.H. L. I. Hsieh, W. P. Gao, J. Yang, B. V. Merinov, W. Xue, Z. Y. Liu, J. X. Zhou, Z. T. Luo, X. Q. Pan, F. Zaera, J. H. Guo, X. F. Duan, W. A. Goddard and Y. Huang, *Matter,* 2020*,* **3**, 1774.
25. T. Y. Yoo, J. M. Lee, S. J. Kim, M. Her, S. Y. Kim, Y. H. Lee, H. Shin, H. Jeong, A. K. Sinha, S. P. Cho, Y. E. Sung and T. Hyeon, Tailoring a three-phase microenvironment for high-performance oxygen reduction reaction in proton exchange membrane fuel cells, *Energy Environ. Sci.,* 2023*,* **16**, 1146.
26. C. Ding, Z. J. Mao, J. S. Liang, X. X. Qin, Q. Zhang, F. Yang, Q. Li and W. B. Cai, Aqueous phase approach to Au-modified Pt-Co/C toward efficient and durable cathode catalyst of PEMFCs, *J. Phys. Chem. C,* 2021, **125**, 23821.